Sensor applications

Localization of Embedded Sensors in Reinforced Concrete via Time-Series Magnetic Field Sensing and Maximum Likelihood Estimation

Ryosuke Sada[1], Toshihisa Tanaka[1], Hisafumi Asaue[2], Tomoki Shiotani[2], Masanori Hashimoto[1]*, and Ryo Shirai[1]**

[1] *Graduate School of Informatics, Kyoto University, Kyoto 606-8501, Japan*
[2] *Office of Institutional Advancement and Communications, Kyoto University, Kyoto 615-8245, Japan*
* *Senior Member, IEEE*
** *Member, IEEE*

Manuscript received 30 April 2025; revised 16 June 2025; accepted 29 June 2025. Date of publication 3 July 2025; date of current version 18 July 2025.

Abstract—To facilitate nonintrusive inspection of aging road infrastructure, we propose a framework in which sensors are embedded in reinforced concrete during construction and later interrogated by a passing inspection vehicle. Precise localization of these sensors, despite limited power and time windows, is crucial to realize this concept. This letter introduces a localization method that exploits time-series magnetic-field signatures captured as a moving anchor passes overhead. Coarse positions are first derived from sequential sensor data, then iteratively refined through maximum-likelihood estimation with distance-weighted confidence. Experiments indicate that the proposed method reduces localization error by 23%–43% relative to conventional techniques, such as simple averaging or nearest-anchor-based estimation, even when the minimum anchor-sensor gap reaches 1 m, underscoring its promise for drive-by infrastructure monitoring without fixed anchors or lane closures.

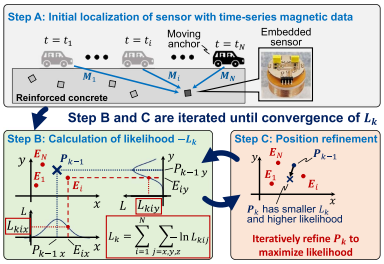

Index Terms—Sensor applications, magnetic field, maximum-likelihood estimation, sensor localization, time-series data.

I. INTRODUCTION

For over a century, reinforced concrete (RC) has served as a common material for constructing bridge deck slabs, thanks to its favorable mechanical properties and cost effectiveness; yet over time, deterioration, such as cracking and delamination emerges, requiring regular inspections for structural integrity. Conventional inspection methods—such as visual inspection, hammer sounding, and chain dragging [1]—are labor-intensive and highly dependent on skilled personnel. They often necessitate lane closures, disrupting traffic. A shrinking pool of skilled inspectors further underscores the need for autonomous and scalable inspection systems [2], [3].

To address these challenges, we propose and are developing an autonomous inspection platform that embeds sensors in RC during construction and enables crack monitoring and condition assessment via a drive-by inspection vehicle. As illustrated in Fig. 1, the system comprises four key components: 1) wireless power transfer (WPT), 2) wireless communication, 3) crack detection, and 4) sensor localization. Among these components, WPT is required because the embedded sensors are inaccessible after construction and therefore cannot rely on batteries. The WPT is typically based on magnetic induction and delivers energy over several tens of centimetres from a coil mounted on the inspection vehicle, thereby ensuring maintenance-free sensor operation. However, since the received power depends on the sensor's location within the RC, energy availability may be limited. Conventional protocols, such as Wi-Fi [4], [5], [6] and Bluetooth Low Energy [7], [8], [9], require high-power oscillators for carrier generation,

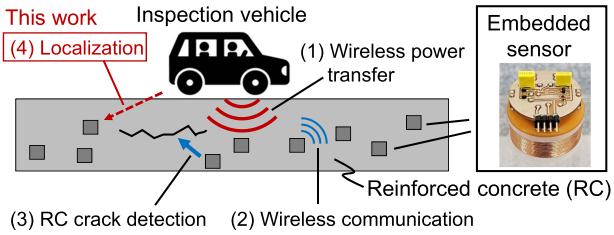

Fig. 1. Overview of the proposed RC crack detection framework.

making them unsuitable under such constraints. To address this, our previous work [10] proposed an ultralow-power method that modulates the reflection of magnetic fields used for WPT, eliminating the need for active carrier generation.

For crack detection, acoustic emission-based techniques have been widely investigated [11], [12], [13] and are readily applicable to this system. These techniques directly capture elastic waves generated in the vicinity of cracks, making them suitable for structural health monitoring.

In contrast to the abovementioned components, accurate localization of embedded sensors remains challenging. Vision-based methods are infeasible because of the lack of line-of-sight within RC, and radio-frequency approaches [14], [15], [16] are constrained by signal distortion arising from steel reinforcement. As an alternative, magnetic field-based methods have been actively studied. Magnetic field-based techniques can be categorized into ac and dc methods. AC magnetic fields are easily distorted by conductive materials [17], such as steel reinforcement, making them unsuitable for accurate localization in RC environments.

DC magnetic fields are scarcely influenced by conductive materials and offer millimeter-level localization accuracy [18], [19]. Our

Corresponding author: Ryo Shirai (e-mail: shirai@i.kyoto-u.ac.jp).
Associate Editor: Sebastian Bader.
This work is supported by JSPS KAKENHI.
Digital Object Identifier 10.1109/LSENS.2025.3585932

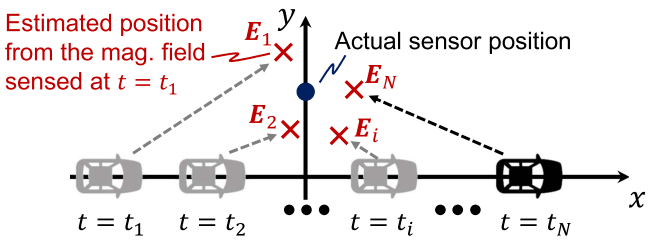

Fig. 2. Iterative localizations using time-series data of magnetic fields generated by an anchor coil mounted on a moving vehicle.

previous work proposed a method to suppress interference from ferromagnetic components [20], making it well suited to RC environments. However, it assumes repeated measurements in a stationary state, which is impractical when the anchor is mounted on a moving vehicle. Although maximum-likelihood methods with multiple fixed anchors have been studied [21], localization using a single moving anchor remains unexplored. This work fills that gap by proposing a maximum-likelihood localization method based on time-series magnetic measurements for RC-embedded sensors.

II. PROPOSED METHOD

This section proposes a localization method for embedded sensors in RC, leveraging time-series magnetic field sensing. In the proposed inspection framework, as illustrated in Fig. 1, a convoy of inspection vehicles travels over the road surface where sensors are embedded within RC structures. The leading vehicle wirelessly supplies power, synchronizes sensor clocks, and instructs sensors when to perform sensing. As the anchor-equipped vehicle passes, each sensor records magnetic field measurements as time-series data and transmits them to a following vehicle for localization. The proposed localization method comprises three steps: (A) initial coarse localization, (B) likelihood computation based on past estimates and observations, and (C) iterative position refinement. Repeat Steps (B) and (C) until convergence, enabling robust localization under noisy conditions.

A. Initial Localization From Time-Series Magnetic Field Data

Fig. 2 illustrates the concept of time-series sensing, where a sensor embedded in RC records the magnetic field $\mathbf{M}_i$ generated by a moving anchor coil at each time step $t = t_i$ $(i = 1, 2, \ldots, N)$ as the inspection vehicle passes by. Based on the sensed magnetic field $\mathbf{M}_i$ at time t_i, an estimated position $\mathbf{E}_i$ is computed by the inspection vehicle that receives the time-series data from the sensor based on our previously proposed localization method [18]. Here, the method in [18] was developed for free-space localization and could suffer from magnetic materials, such as steel reinforcement in RC. However, its successive work [20] reported that the effect of magnetic materials, whose positions are known, can be analytically compensated. Since the placement of reinforcement bars is predetermined during construction, their influence can be mitigated by Tanaka et al. [20]. Consequently, to focus on the core methodological contribution of this work, the following considers a simplified scenario without reinforcement.

Due to the high level of noise in the magnetic sensor output, each estimate $\mathbf{E}_i$ tends to deviate significantly from the true sensor position, as illustrated in Fig. 2. To mitigate this error in successive step, we first compute the centroid of the estimated positions, defined as $\mathbf{P}_0 = \frac{1}{N}\sum_{i=1}^{N}\mathbf{E}_i$, and adopt it as the output of this initial localization step.

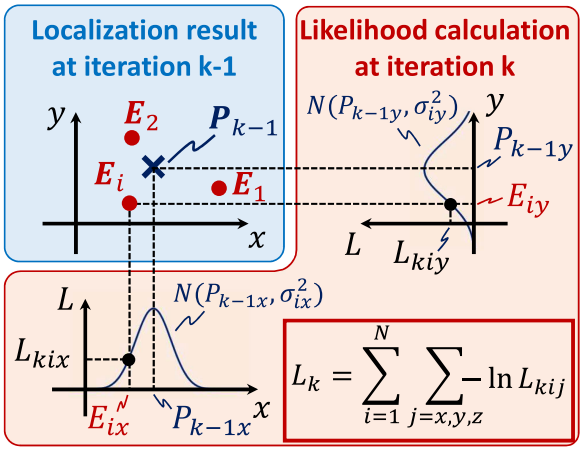

Fig. 3. Likelihood calculation based on the localization result at the previous iteration.

B. Likelihood Computation From Previous Estimate

This step and the next (Step C) are repeated until the estimated sensor position converges. In the kth iteration, the likelihoods $L_1, \ldots, L_N$ of the coarse estimates $\mathbf{E}_1, \ldots, \mathbf{E}_N$ are computed based on the previous estimate $\mathbf{P}_{k-1}$. The overall process is illustrated in Fig. 3. As will be introduced in the following section, the estimation error increases with the distance between the anchor coil position $\mathbf{A}_i$ at time $t = t_i$ and the sensor position. Accordingly, the distance r between $\mathbf{A}_i$ and the previous estimate $\mathbf{P}_{k-1} = (P_{k-1x}, P_{k-1y}, P_{k-1z})$ is computed as $r = |\mathbf{A}_i - \mathbf{P}_{k-1}|$. Using this distance r, the standard deviations $\boldsymbol{\sigma}_i = (f_x(r), f_y(r), f_z(r))$ of the estimation error in each coordinate are obtained based on empirical functions f_x, f_y, and f_z, preconstructed from measured data. Then, the negative log-likelihood L_{ki} at time $t = t_i$ is computed as follows:

$$L_{ki} = \sum_{j\in\{x,y,z\}} \mathcal{N}(E_{ij}; P_{k-1j}, \sigma_{ij}^2) \tag{1}$$

where $\mathcal{N}(x; \mu, \sigma^2)$ denotes the probability density of a normal distribution with mean μ and variance σ^2, evaluated at x. Finally, the total negative log-likelihood L_k for the kth iteration is calculated by summing over all time steps: $L_k = \sum_{i=1}^{N} L_{ki}$.

C. Position Update Based on Likelihood

In this step, the estimated sensor position $\mathbf{P}_k$ is updated to minimize the negative log-likelihood L_k computed in Step B. Various optimization techniques can be used for this purpose. For example, using a gradient descent method, the update rule is given by $\mathbf{P}_k = \mathbf{P}_{k-1} - \alpha(\frac{\partial L_k}{\partial x}, \frac{\partial L_k}{\partial y}, \frac{\partial L_k}{\partial z})$, where α is a step-size parameter controlling the update magnitude.

Unlike simple averaging, the proposed method uses reliability-based weighting derived from a Gaussian noise model, emphasizing more trustworthy observations—typically those obtained when the anchor is closer—and thereby achieving higher accuracy under heterogeneous noise.

III. EVALUATION AND DISCUSSION

A. Setup

Fig. 4 shows the experimental setup, including the dimensions of the anchor coil, the magnetic sensor, and the gimbal used to align the sensor. The magnetic field was measured over a 600 mm × 1000 mm

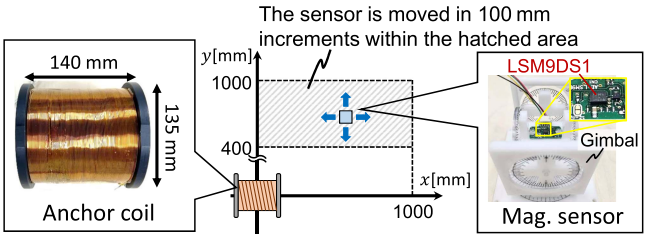

Fig. 4. Experimental setup.

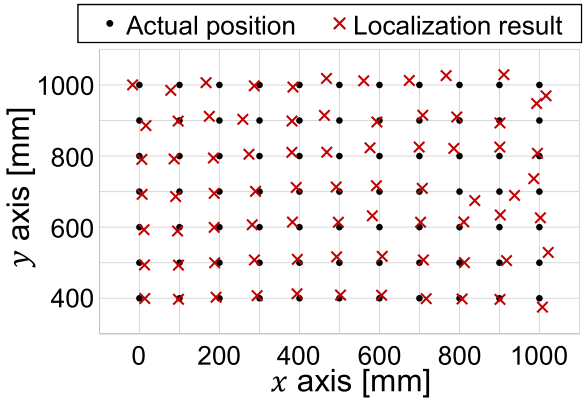

Fig. 5. Localization result using a stationary anchor.

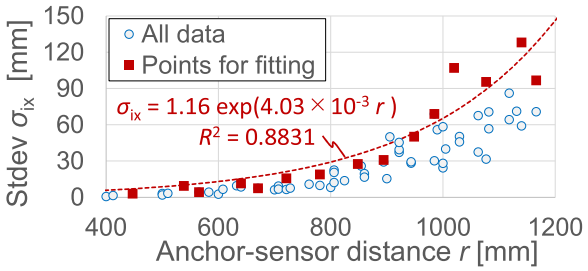

Fig. 6. Standard deviation of the fixed base station estimation results with respect to the *x*-axis.

area in 100 mm increments. The sensor used was the LSM9DS1 from STMicroelectronics and was mounted on the gimbal to maintain consistent height and orientation relative to the coil. To isolate the magnetic field generated by the coil, we subtracted the sensor output measured with no current from that with 3 A applied to the coil, which produced approximately 80 mT at the coil center. Localization was then performed using the method proposed in [18]. Referring to [18], which shows axial symmetry of the magnetic field around the coil, we limited the evaluation to a 2-D plane to simplify the experiment without loss of generality.

B. Localization Accuracy With a Stationary Anchor

This section evaluates the localization accuracy using a stationary anchor varying the sensor position. Fig. 5 shows the mean of 1000 localization trials for each sensor position. Each trial involved estimating the sensor position from a single magnetic field measurement using the method proposed in [18]. The ground truth sensor positions were determined based on predefined 100 mm grid points marked on the test surface. These positions served as the reference for evaluating localization error. As the results indicate, accuracy is the highest near the origin where the anchor coil is located. This supports the modeling of f_x, f_y, and f_z as functions of anchor-sensor distance r.

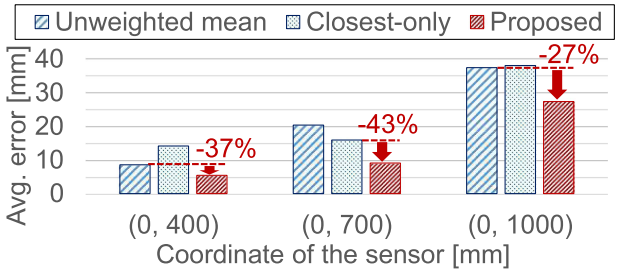

Fig. 7. Localization error at three sensor positions using time-series data from a moving anchor.

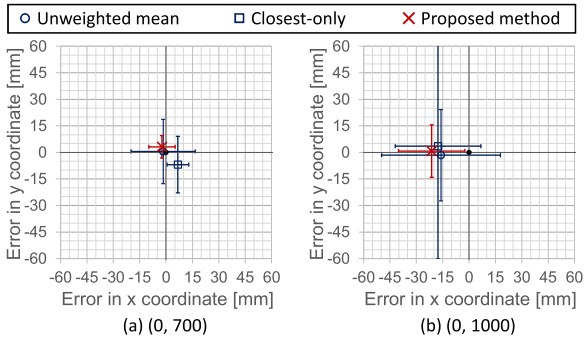

Fig. 8. Distributions of estimated positions at two sensor locations. (a) (0, 700). (b) (0, 1000).

To determine f_x and f_y, we evaluated the standard deviation of estimation errors $\boldsymbol{\sigma}_i$ as a function of r. Fig. 6 shows the results for the x-axis; the y-axis exhibited similar trends. Although some fluctuation exists, the standard deviation generally increases with distance. We fitted worst-case curves to the maximum values in each interval of r [mm], yielding

$$\sigma_{ix} = f_x(r) = 1.16 \times \exp(4.03 \times 10^{-3} r) \text{ [mm]} \quad (2)$$

$$\sigma_{iy} = f_y(r) = 5.55 \times 10^{-1} \times \exp(4.73 \times 10^{-3} r) \text{ [mm]}. \quad (3)$$

C. Localization With a Moving Anchor

This section evaluates the proposed method using time-series magnetic data corresponding to an anchor moving from $x = -500$ to $x = 500$ mm at 36 km/h, sampled at 100 Hz (i.e., 100 mm per sample). To simplify the experiment, we fixed the anchor and moved the sensor in 100 mm steps along the x-axis to simulate the same relative motion. DC magnetic measurement data were used under the assumption of quasi-static conditions, which is valid in this context. As the anchor coil is fixed relative to the vehicle, eddy currents are not induced in the vehicle body. RC reinforcement bars are rod-shaped and rarely form current loops, and hence eddy currents in them are negligible. Therefore, the quasi-static assumption holds. The sensor was placed from (0, 400) to (0, 1000) mm in 100 mm steps. For comparison, two baseline methods were implemented: 1) simple averaging over 11 time points and 2) single-point estimation at the closest anchor approach ($x = 0$). Each evaluation was repeated 1000 times with measured data.

Fig. 7 shows that the proposed method reduces localization error by 23%–43% across all cases. Fig. 7 illustrates representative cases with the sensor located at (0, 400), (0, 700), and (0, 1000) mm, showing that the error increases with distance, but the proposed method consistently outperforms the baselines. Fig. 8 shows error distributions for (0, 700) and (0, 1000) mm. The markers indicate the mean of each distribution, which does not necessarily correlate with lower mean error. Error bars represent standard deviations, revealing that while the mean positions

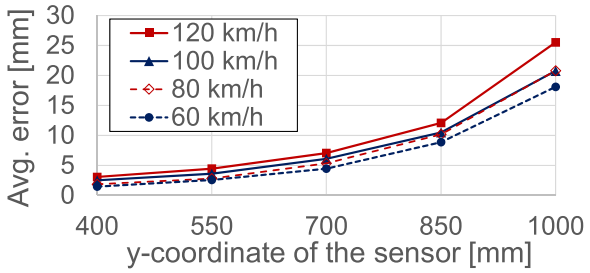

Fig. 9. Average localization error versus sensor *y*-coordinate at different inspection vehicle speeds.

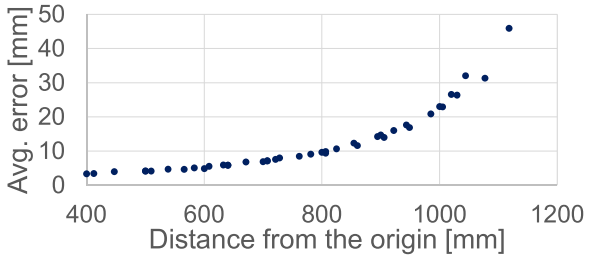

Fig. 10. Localization error versus distance from the origin in 3-D simulations with varying sensor depth.

are comparable, the proposed method exhibits reduced variance, leading to improved average accuracy.

D. Impact of Anchor Speed on Localization Accuracy

To enable drive-by inspection without lane closures, localization performance at higher anchor speeds must be evaluated. Section III-C addressed 36 km/h; here we simulate speeds from 60 to 120 km/h using measured magnetic field data.

The sensor was fixed along the y-axis while the anchor moved along x. For each speed, we assume that one sample is acquired every 1 ms (i.e., at 1 kHz, the maximum supported by the LSM9DS1), and use 51 time-series samples per trial. The anchor position at each sample time was calculated based on its speed (e.g., at 100 km/h, the anchor moves approximately 27.8 mm per 1 ms). A higher speed results in more samples being taken at positions farther from the sensor, where the magnetic field is weaker and noisier, leading to greater estimation error. Fig. 9 shows that accuracy degrades with speed, particularly at larger anchor-sensor distances. These results highlight the importance of limiting the y-range per anchor based on the required localization accuracy.

E. Impact of Sensor Burial Depth on Localization Accuracy

Sections III-C and D evaluated localization in a 2-D plane at $z = 0$ and omitted 3-D evaluation, based on the assumption from [18] that accuracy depends mainly on anchor-to-sensor distance, rather than depth. To validate this, we conducted 3-D localization by varying y from 0 to 1000 mm and z from -500 to 0 mm in 100 mm steps.

Fig. 10 confirms that error is determined primarily by distance rather than depth, supporting the generality of the 2-D evaluation in earlier sections.

IV. CONCLUSION

To actualize autonomous, drive-by monitoring of RC structures with embedded sensors, this letter presented a maximum likelihood-based localization method utilizing noisy time-series magnetic field data from a moving anchor. The proposed approach iteratively integrates sequential observations, weighted by empirically modeled confidence, to refine position estimates. Experimental validation showed consistent improvements over single-point estimation, with localization error reduced by 23%–43%. While this study focused on scenarios without steel reinforcement to isolate core performance, the method is expected to be applicable to RC environments with known steel layouts by incorporating compensation techniques, such as [20], enabling practical application to RC structures.

ACKNOWLEDGMENT

This work was supported by JSPS KAKENHI under Grant JP25K21172.

REFERENCES

[1] *Standard Practice for Measuring Delaminations in Concrete Bridge Decks by Sounding*, ASTM Standard D4580/D4580M-12, 2018.
[2] D. E. Bloom, D. Canning, and G. Fink, "Implications of population ageing for economic growth," *Oxford Rev. Econ. Policy*, vol. 26, no. 4, pp. 583–612, 2010.
[3] D. Acemoglu and P. Restrepo, "Demographics and automation," *Rev. Econ. Stud.*, vol. 89, no. 1, pp. 1–44, 2022.
[4] W. Hlaing, S. Thepphaeng, V. Nontaboot, N. Tangsunantham, T. Sangsuwan, and C. Pira, "Implementation of WiFi-based single phase smart meter for Internet of Things (IoT)," in *Proc. Int. Elect. Eng. Congr.*, 2017, pp. 1–4.
[5] H. Lakdawala et al., "A 32 nm SoC with dual core ATOM processor and RF WiFi transceiver," *IEEE J. Solid-State Circuits*, vol. 48, no. 1, pp. 91–103, Jan. 2013.
[6] M. Hernandez-Aguila, J.-L. Olvera-Cervantes, A.-E. Perez-Ramos, and A. Corona-Chavez, "WiFi sensor-node with high sensitivity and linearity based on a quarter-wavelength resonator for measuring crack width," *IEEE Sensors J.*, vol. 23, no. 23, pp. 28883–28890, Dec. 2023.
[7] R. Tei, H. Yamazawa, and T. Shimizu, "BLE power consumption estimation and its applications to smart manufacturing," in *Proc. 54th Annu. Conf. Soc. Instrum. Control Engineers Jpn.*, 2015, pp. 148–153.
[8] O. Nouali et al., "A BLE-based data collection system for IoT," in *Proc. 1st Int. Conf. New Technol. Inf. Commun.*, 2015, pp. 1–5.
[9] G. Loubet, A. Sidibe, A. Takacs, and D. Dragomirescu, "Battery-free bluetooth low energy sensing nodes for structural health monitoring of concretes," in *Proc. 13th Int. Workshop Struct. Health Monit.*, 2022, pp. 1–9, doi: 10.12783/shm2021/36247.
[10] R. Fukugasako, H. Asaue, T. Shiotani, M. Hashimoto, and R. Shirai, "A current chopper-assisted magnetic field-based backscatter communication method with WPT overcoming ultra-low coupling coefficients," *IEEE Sensors J.*, vol. 25, no. 10, pp. 18249–18256, May 2025.
[11] H. Takamine, K. Watabe, H. Miyata, H. Asaue, T. Nishida, and T. Shiotani, "Efficient damage inspection of deteriorated RC bridge deck with rain-induced elastic wave," *Construction Building Mater.*, vol. 162, pp. 908–913, 2018.
[12] T. Shiotani, T. Nishida, H. Asaue, and Y. Kobayashi, "Interpretation of fatigue damage evolution in RC slabs by means of innovative 3D AE tomography," in *Proc. 9th Int. Conf. Fracture Mechan. Concrete Concrete Struct.*, vol. 2, May 2016, pp. 1–12, doi: 10.21012/FC9.225.
[13] T. Shiotani, H. Asaue, T. Nishida, T. Maeshima, and Y. Tanaka, "Evolution of fatigue damage in wheel-loading tests evaluated by 3D elastic-wave tomography," *J. Disaster Res.*, vol. 12, no. 3, pp. 487–495, 2017.
[14] S. He and S.-H. G. Chan, "Wi-Fi fingerprint-based indoor positioning: Recent advances and comparisons," *IEEE Commun. Surv. Tut.*, vol. 18, no. 1, pp. 466–490, Firstquarter 2016.
[15] C. Yang and H.-R. Shao, "WiFi-based indoor positioning," *IEEE Commun. Mag.*, vol. 53, no. 3, pp. 150–157, Mar. 2015.
[16] C. Wu, Z. Yang, Y. Liu, and W. Xi, "WILL: Wireless indoor localization without site survey," *IEEE Trans. Parallel Distrib. Syst.*, vol. 24, no. 4, pp. 839–848, Apr. 2013.
[17] V. Pasku et al., "Magnetic field-based positioning systems," *IEEE Commun. Surv. Tut.*, vol. 19, no. 3, pp. 2003–2017, thirdquarter 2017.
[18] R. Shirai and M. Hashimoto, "DC magnetic field based 3D localization with single anchor coil," *IEEE Sensors J.*, vol. 20, no. 7, pp. 3902–3913, Apr. 2020.
[19] R. Shirai, Y. Itoh, and M. Hashimoto, "Make it trackable: An instant magnetic tracking system with coil-free tiny trackers," *IEEE Access*, vol. 9, pp. 26616–26632, 2021.
[20] T. Tanaka, R. Shirai, and M. Hashimoto, "DC magnetic field-based analytical localization robust to known stationary magnetic object," in *Proc. IEEE 65th Int. Midwest Symp. Circuits Syst.*, 2022, pp. 1–4.
[21] A. Poulose, Ž. Emeršič, O. S. Eyobu, and D. Seog Han, "An accurate indoor user position estimator for multiple anchor UWB localization," in *Proc. Int. Conf. Inf. Commun. Technol. Convergence*, 2020, pp. 478–482.